PHYSICSAccess Research Paper
ISSN Online: 2756-3898, ISSN Print: 2714-500X https://doi.org/10.47514/phyaccess.2026.6.2.021

Influence of Annealing Atmosphere on the Structural, Morphological, Optical, and Photoluminescence Properties of Hydrothermally Synthesized MoS_2 Nanopowders

Bunmi J Akeredolu[1, 2, 3], John F Wansah[1, 3], Yusuf Sani[1], Michael O Awoji[1], Eli Danladi[4], Asabe M Magomya[3, 5], Peverga R Jubu[6], Michael B Ochang[6], and Lehlohonolo F Koao[2]

[1] Department of Pure and Applied Physics, Faculty of Physical Science, Federal University Wukari, PMB 1020, Taraba State. Nigeria
[2] Department of Physics, University of the Free State, 9866, Phuthaditjhaba, South Africa
[3] Centre for Energy Research, Federal University Wukari, PMB 1020, Taraba State, Nigeria
[4] Department of Physics, Federal University of Health Sciences, Otukpo, P.M.B. 145, Nigeria
[5] Department of Chemistry, Faculty of Physical Science, Federal University, Wukari, PMB 1020, Taraba State, Nigeria
[6] Department of Industrial Physics, Joseph Sarwuan Tarka University, Makurdi, Nigeria

Corresponding E-mail: akeredolu@fuwukari.edu.ng

Received 27-09-2026
Accepted for publication 10-11-2026
Published 17-11-2026

Abstract

Molybdenum disulfide (MoS_2) is a layered semiconductor whose structural and optical properties are sensitive to thermal processing. In this study, hydrothermally synthesised MoS_2 nanopowders were annealed at 500 °C for 2 h under flowing nitrogen (N_2) or argon (Ar), and characterised using X-ray diffraction (XRD), Raman and Fourier-transform infrared (FTIR) spectroscopy, scanning and transmission electron microscopy (SEM/TEM), ultraviolet–visible spectroscopy, and photoluminescence (PL). XRD confirmed the hexagonal 2H-MoS_2 phase, with mean Scherrer crystallite sizes of 4.97 nm (N_2) and 4.67 nm (Ar). Raman peak separations of 24.9 cm^{-1} (N_2) and 25.0 cm^{-1} (Ar) indicated multilayer-like vibrational responses. Both powders exhibited aggregated, irregular flake-like morphologies, with mean TEM particle sizes of 13.30 nm (N_2) and 17.97 nm (Ar) for the selected particles. The N_2-annealed sample showed higher measured absorbance and a smaller apparent direct-transition optical band gap (1.62 eV) than the Ar-annealed sample (1.80 eV), whereas the Ar-annealed sample exhibited higher PL intensity under identical excitation conditions. These findings demonstrate that the post-synthesis annealing atmosphere influences the structural, morphological, and optical properties of MoS_2 nanopowders, which may have potential for hydrogen evolution reaction applications.

Keywords: Molybdenum disulfide; hydrothermal synthesis; annealing atmosphere; photoluminescence; nanopowders.

I. Introduction

Molybdenum disulfide (MoS_2), a representative transition-metal dichalcogenide (TMD), has attracted considerable research interest because of its layered structure and tunable optical and electronic properties [1–3]. Each structural unit consists of a molybdenum plane sandwiched between two sulfur planes, forming an S–Mo–S layer. Adjacent layers are held together by relatively weak van der Waals interactions [4]. The common semiconducting 2H phase exhibits pronounced dimensionality-dependent electronic behaviour: bulk-like MoS_2 has an indirect band gap of approximately 1.2–1.3 eV, whereas an isolated monolayer exhibits a direct optical transition near 1.8–1.9 eV [5]. Consequently, interlayer coupling, phonon confinement, strain, disorder, and surface electronic states can influence its optical absorption and photoluminescence (PL) [6–7]. Understanding how synthesis conditions and thermal processing affect these properties is important for the development of photodetectors, sensors, nanoelectronics and energy-related devices [8–9].

MoS_2 can be prepared using top-down approaches, such as mechanical and liquid-phase exfoliation, or bottom-up techniques, including chemical vapour deposition, physical vapour deposition, atomic layer deposition, and hydrothermal or solvothermal synthesis [9–10]. Although exfoliation can produce thin flakes, their lateral dimensions and thicknesses may be heterogeneous. In contrast, vapour-phase methods can produce controlled films but often require specialised equipment and carefully regulated growth environments. Reference [11], for example, demonstrated that solvent selection influences the yield and structural preservation of liquid-phase-exfoliated MoS_2. Hydrothermal synthesis has attracted attention because it facilitates precursor dissolution, nucleation, and crystal growth in a sealed aqueous environment without requiring vacuum processing. Reaction temperature, duration, and precursor chemistry provide practical means of controlling particle formation, although aggregation, residual precursor species, and relatively long reaction times may require further optimisation [9], [12–13]. Its relatively straightforward powder preparation and accessible processing conditions motivated the hydrothermal approach adopted in this study.

Previous experimental studies have demonstrated that hydrothermal synthesis conditions can influence the morphology and optical properties of MoS_2. Reference [14] obtained MoS_2 nanosheets and nanoflowers by varying the synthesis temperature and associated the resulting structural differences with changes in the band gap, while [15] reported hydrothermally synthesised MoS_2 nanoparticles with hexagonal diffraction features, flower-like morphologies and an apparent direct optical band gap of approximately 1.80 eV. Similarly, [16] investigated the effects of hydrothermal reaction time on few-layer MoS_2 nanoflowers and reported variations in structural strain and optical transition energies ranging from approximately 1.56 to 1.63 eV. These findings demonstrate that synthesis conditions, morphology, and structural ordering can influence the measurable properties of MoS_2. However, post-synthesis annealing conditions also warrant investigation because powders obtained from the same synthesis batch may exhibit different structural, vibrational, and optical responses following heat treatment under different atmospheres.

Annealing provides thermal energy that can promote lattice relaxation, crystallite restructuring, and the redistribution of surface-bound species [5]. The surrounding atmosphere may also influence the availability of reactive species and the thermodynamic or kinetic pathways associated with defect formation [17]. Even when nominally inert gases such as argon and nitrogen are used, differences in the resulting material do not necessarily imply the direct incorporation of nitrogen into the MoS_2 structure. Gas-dependent thermal transport, residual oxygen or moisture, sulfur loss, and variations in the surface environment may also contribute. Reference [18] reported sulfur-vacancy-related photoluminescence features following the thermal treatment of monolayer MoS_2 in an Ar/H_2 atmosphere, while [19] investigated sputtered MoS_2 films subjected to vacuum or nitrogen-plasma treatment. References [20–21] further demonstrated that oxygen annealing and other post-deposition treatments can modify the luminescence and optoelectronic properties of MoS_2 monolayers. Although these studies establish the sensitivity of MoS_2 to processing conditions, differences in material morphology and treatment environments limit their direct applicability to hydrothermally synthesised nanopowders.

Regardless of these advances, a direct comparison of flowing N_2 and Ar annealing applied to a common batch of hydrothermally synthesised MoS_2 powder under otherwise identical thermal conditions remains necessary. Previous studies have largely focused on optimising synthesis parameters or investigating post-treatment effects in films and monolayers. Comparatively fewer studies have examined the relationship between powder X-ray diffraction (XRD) parameters and Raman vibrational modes alongside Fourier-transform infrared (FTIR) features, scanning and transmission electron microscopy (SEM/TEM) observations, optical absorption and steady-state PL under these two annealing atmospheres. Such complementary characterisation techniques can provide a broader understanding of processing-related property changes. However, these measurements alone cannot uniquely quantify sulfur-vacancy concentrations, determine non-radiative carrier lifetimes, or establish catalytic activity. A systematic, measurement-based comparison is therefore required to distinguish experimentally observed changes from possible physical explanations that require further investigation.

Accordingly, this study investigates the influence of N_2 and Ar annealing on the crystallographic, morphological, vibrational and optical properties of hydrothermally synthesised MoS_2 nanopowders. Ammonium molybdate

tetrahydrate and thiourea were subjected to hydrothermal treatment at 200 °C for 24 h. The resulting material was divided into two portions and annealed at 500 °C for 2 h under the respective flowing gases. XRD was employed to examine the diffraction features and estimate crystallite sizes using the Scherrer equation; Raman spectroscopy was used to investigate the in-plane and out-of-plane vibrational modes; and FTIR spectroscopy was used to examine vibrational signatures and surface-associated species. SEM and TEM were used to investigate the morphology, while ultraviolet–visible (UV–Vis) and PL spectroscopy were employed to examine optical absorption, apparent optical band gaps, and radiative emission. The novelty of this study lies in applying these complementary characterisation techniques to powders obtained from the same precursor batch and subjected to identical annealing temperatures and durations under N_2 and Ar atmospheres. This approach enables the influence of the annealing atmosphere to be assessed while minimising differences associated with the synthesis route. The study establishes comparative material-property trends, while the potential application of the materials in hydrogen evolution is considered as motivation for future electrochemical or photoelectrochemical investigations.

II. Experimental Procedure

A. Materials

All chemicals used in this study were analytical-reagent (AR) grade and were used without further purification. Ammonium molybdate tetrahydrate [$(NH_4)_6M_7O_{24}\cdot4H_2O$, 99%] and thiourea [$CS(NH_2)_2$, 99%] were purchased from Minema, South Africa, and used as the molybdenum and sulfur precursors, respectively. Deionised water obtained from the Central Laboratory, Federal University Wukari, was used as the solvent.

B. Synthesis of MoS_2 Nanopowders

MoS_2 nanopowders were synthesised using the hydrothermal method. First, 1.00 g of ammonium molybdate tetrahydrate was dissolved in 60 mL of deionised water and magnetically stirred for 15 min to obtain a homogeneous solution. Subsequently, 3.00 g of thiourea was gradually added under continuous stirring until a uniform mixture was obtained. The resulting solution was transferred into a 100 mL Teflon-lined stainless-steel autoclave. The reaction mixture occupied approximately 60% of the autoclave's total capacity. The autoclave was sealed and maintained at 200 °C for 24 h.

After the autoclave had cooled to room temperature, the resulting black precipitate was collected by centrifugation, repeatedly washed with deionised water and ethanol, and dried at 80 °C for 12 h.

The dried powder was divided into two equal portions for subsequent annealing. High-purity nitrogen (99.9%) and argon (99.9%) were used as the respective annealing atmospheres to minimise exposure to ambient oxygen. Before heating, the furnace tube (programmable 1600 °C horizontal tube furnace, BR-NT, Zhengzhou Brother Furnace Co., Ltd., China) was purged with the corresponding gas for 30 min to remove residual air and oxygen. A constant gas flow rate of 100 sccm was maintained throughout heating, annealing, and cooling. For both treatments, the temperature was increased to 500 °C at a heating rate of 5 °C min^{-1} and maintained at this temperature for 2 h. The samples were subsequently allowed to cool naturally under their respective gas atmospheres. The resulting powders are designated MoS_2-N_2 and MoS_2-Ar. The overall synthesis and annealing procedure used to prepare the MoS_2 nanopowders is schematically illustrated in Fig. 1.

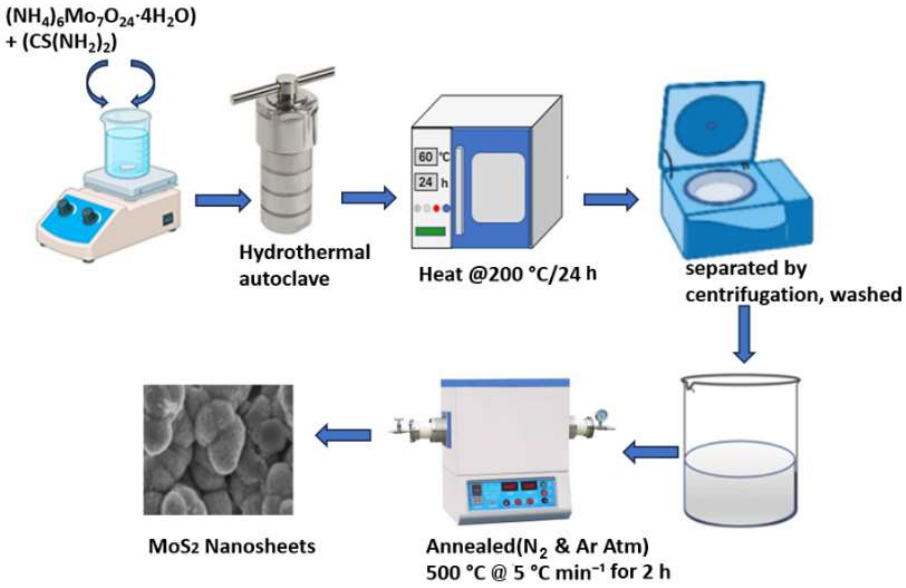


Fig. 1. Schematic illustration of the synthesis and annealing workflow used to prepare the MoS_2 nanopowders.

For optical characterisation, 10 mg of each MoS_2 nanopowder was ultrasonically dispersed in 10 mL of an isopropyl alcohol (IPA)–water mixture prepared at a ratio of 7:3. The resulting dispersion had a concentration of 1 mg mL^{-1}. A volume of 5 µL of the dispersion was deposited onto glass substrates by drop casting. The deposited films were dried at 150 °C for 2 h to remove residual solvent and moisture. This treatment was intended solely for drying the deposited films and was not intended as an additional annealing step. The same film-preparation and drying conditions were applied to both nitrogen- and argon-annealed samples to ensure consistency.

C. Characterisation

The crystal structure and diffraction peak broadening were examined using an X-ray diffractometer (XRD; Bruker D8 Advance, Germany) with Cu Kα radiation (λ = 1.5406 Å). Data were collected over a 2θ range of 10–90° using a step size of 0.026°.

Surface morphology and lateral dimensions were examined using a field-emission scanning electron microscope (FE-SEM; JEOL JSM-7600F) operated at an accelerating voltage of 5 kV in InLens mode, with a working distance of 18 mm. Further morphological characterisation was performed using a Titan Themis 300 transmission electron microscope (TEM) operated at an accelerating voltage of 200 kV. For TEM analysis, the samples were dispersed in ethanol and deposited onto carbon-coated copper grids.

Fourier-transform infrared (FTIR) spectra were acquired using a PerkinElmer 300mx FTIR spectrometer over the wavenumber range of 4400–350 cm^{-1} at a resolution of 4 cm^{-1}. The vibrational modes of the samples were investigated at room temperature using a Horiba LabRAM HR Raman spectrometer. Measurements were performed using linearly polarised laser light at 532 nm, with the laser power maintained below 1 mW to minimise possible laser-induced effects. An 1800-groove mm^{-1} grating was used, providing an instrumental resolution of approximately 0.5 cm^{-1}. The laser was focused onto the samples to a spot diameter of approximately 1 µm using a 50× long-working-distance objective lens.

Ultraviolet–visible (UV–Vis) spectra were acquired using a Lambda 950 spectrophotometer (PerkinElmer, USA). The spectra presented in Fig. 3 cover the wavelength range of 300–1000 nm. Room-temperature steady-state photoluminescence (PL) measurements were performed using a Varian Cary Eclipse fluorescence spectrophotometer equipped with a 150 W xenon excitation lamp.

III. Results and Discussion

A. Structural analysis

The XRD patterns of hydrothermally synthesized MoS_2 annealed under N_2 and Ar are shown in Fig. 2(a). Both patterns display a strong low-angle reflection at 2θ = 14.65° (N_2) and 14.22° (Ar), consistent with the (002) basal-plane reflection of hexagonal 2H-MoS_2. Reflections near 34° and 59–60° are also consistent with the (100) and (110) families, respectively, of the 2H structure [6], [15]. A weaker feature near 40° is consistent with a higher-index 2H reflection. No prominent additional crystalline-phase peaks are identified in the displayed scan; nevertheless, diffraction alone cannot exclude minor amorphous or low-concentration impurities. The preferred (002) intensity reflects substantial basal-plane stacking or texture but is not, by itself, proof of a superior crystallinity or preferential growth mechanism.

As Fig. 2(b) shows, the Ar-treated powder has the stronger fitted (002) peak under the plotted measurement conditions, whereas the N_2-treated peak occurs at the higher diffraction angle. Bragg's relation, d = λ/(2 sin θ), therefore gives a decrease in d_{002} from 6.223 Å (Ar) to 6.042 Å (N_2), agreeing with the corresponding reduction of the c-axis lattice parameter from 12.430 to 12.120 Å (Table I). This is consistent with a smaller average interlayer repeat spacing after N_2 annealing. The a = b lattice parameters are 3.057 Å (Ar) and 3.042 Å (N_2), suggesting a smaller in-plane metric for the latter sample. These shifts may arise from thermal relaxation, stacking variation, or defect-related lattice changes; without additional composition- and defect-sensitive measurements, a unique microscopic mechanism cannot be assigned [4], [6], [22–24].

Crystallite size (D) was estimated from peak broadening using the Scherrer relation in (2), after converting the full width at half maximum, β, to radians. The mean of the reflection-specific Scherrer values for the apparent crystalline sizes is 4.67 nm for MoS_2-Ar and 4.97 nm for MoS_2-N_2 (Table I), corresponding to an approximately 6.4% larger estimate in the N_2-treated sample. This is a modest change in coherent diffraction-domain size, not a direct measurement of particle diameter or an unambiguous increase in crystallinity. The use of the Scherrer method in this work assumes that instrumental and microstrain broadening are negligible. An independent instrumental broadening correction with a standard reference material was not conducted, and thus, the calculated crystallite sizes are regarded as apparent or estimated crystallite sizes.

The XRD-derived crystallographic parameters are summarized in Table I.

$$\mathrm{d} = \frac{\lambda}{2\,\mathrm{Sin}\,\theta} \tag{1}$$

$$D = \frac{K\lambda}{\beta\cos\theta} \tag{2}$$

$$\frac{1}{d_{hkl}^2} = \frac{4}{3}\frac{h^2+hk+k^2}{a^2} + \frac{l^2}{c^2} \tag{3}$$

$$V = \frac{\sqrt{3}}{2}a^2c = a^2c\,sin120 \tag{4}$$

$$SSA = \frac{6}{D*\rho} \tag{5}$$

$$\delta = \frac{1}{D^2} \tag{6}$$

$$\varepsilon = \frac{\beta}{4\tan\theta} \tag{7}$$

In (1)–(7), λ is the Cu Kα wavelength (1.5406 Å), θ is the Bragg angle, β is the diffraction peak full width at half

maximum in radians, K is the Scherrer shape factor, h, k and l are Miller indices, a and c are hexagonal lattice parameters, ρ is the density assumed in the geometrical surface-area calculation, and D is the estimated coherent-domain size. For a hexagonal unit cell, the correct interplanar-spacing and unit-cell-volume expressions are given in (3) and (4). Equation (5) provides only a geometric estimate of specific surface area (SSA), not a measured Brunauer–Emmett–Teller surface area; its numerical values depend on the density and particle-shape assumptions. The approximate dislocation-density proxy $\delta = 1/D^2$ (see (6)) yields the correct unit of m^{-2} but does not independently count dislocations. The tabulated values decrease from about 0.050×10^{18} m^{-2} for MoS_2-Ar to 0.0454×10^{18} m^{-2} for MoS_2-N_2, consistent with the increase in mean coherent-domain size [22], [25–26].

The tabulated geometric SSA estimates are 260.185 m^2g^{-1} (Ar) and 248.193 m^2g^{-1} (N_2); this difference is consistent with the inverse dependence of the assumed model on D, but does not establish a measured change in accessible surface area. Likewise, the strain parameter calculated using (7) averages approximately 0.0320 for Ar and 0.0319 for N_2 and is dimensionless. It is inappropriate to denote these values as being multiplied by 10^{-3} without corresponding numerical conversion. Since size and strain may both contribute to diffraction peak widths, these quantities should be regarded as approximate estimates pending instrumental-broadening correction and a dedicated line-profile analysis. Taken together, the XRD data support small atmosphere-dependent changes in basal spacing and coherent-domain size; they do not directly establish sulfur-vacancy density or carrier transport.

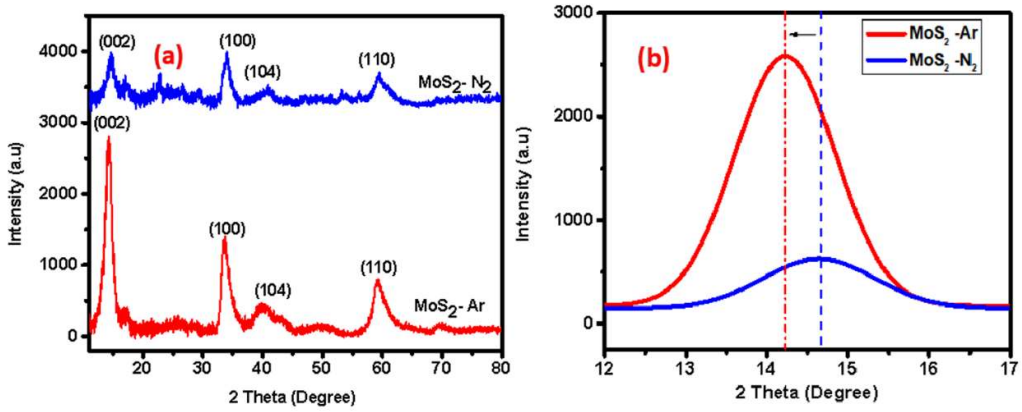


Fig. 2. (a) XRD patterns of MoS_2 nanopowders annealed under N_2 and Ar, and (b) Gaussian fitting of their (002) reflections.

Table I. XRD-derived crystallographic parameters of MoS_2 nanopowders annealed under N_2 and Ar.

Atmosphere	(hkl)	2θ (°)	d_{hkl} (Å)	FWHM β (°)	D (nm)	$a = b$ (Å)	c (Å)	SSA* (m^2 g^{-1})	δ ($\times 10^{18}$ m^{-2})	ε (unitless)
MoS_2-Ar	002	14.22	6.223	1.5344	5.22		12.430	227.16	0.037	0.0537
	100	33.81	2.649	1.6244	5.11	3.057		232.05	0.038	0.0233
	110	59.53	1.552	2.4813	3.69			321.35	0.074	0.0189
Average			3.475		4.67			260.185	0.050	0.0320
MoS_2-N_2	002	14.65	6.042	1.7548	4.56		12.120	260.04	0.0481	0.0596
	100	33.99	2.635	1.3026	6.38	3.042		185.86	0.0246	0.0186
	110	59.71	1.547	2.3069	3.97			298.68	0.0634	0.0175
Average			3.408		4.97			248.193	0.0454	0.0319

B. Surface Profilometry Analysis

Profilometry was used to analyze the surface morphology and thickness of the MoS_2 film synthesized by the hydrothermal method and deposited on a glass substrate. The films were dried at 150 °C for 2 h to eliminate the solvent and moisture in the deposited films. As can be seen in Fig. 3, there is a pronounced difference in level between the substrate and the MoS_2 film area, and the step height is estimated to be approximately 3.0 μm, which corresponds to the film thickness. The surface-height changes clearly seen are attributed to the aggregation of MoS_2 particles and the non-uniformity of the film morphology as a result of non-uniform deposition and irregularities in the solvent evaporation. The results have verified the formation of a measurable MoS_2 film and provided thickness and surface topography information.

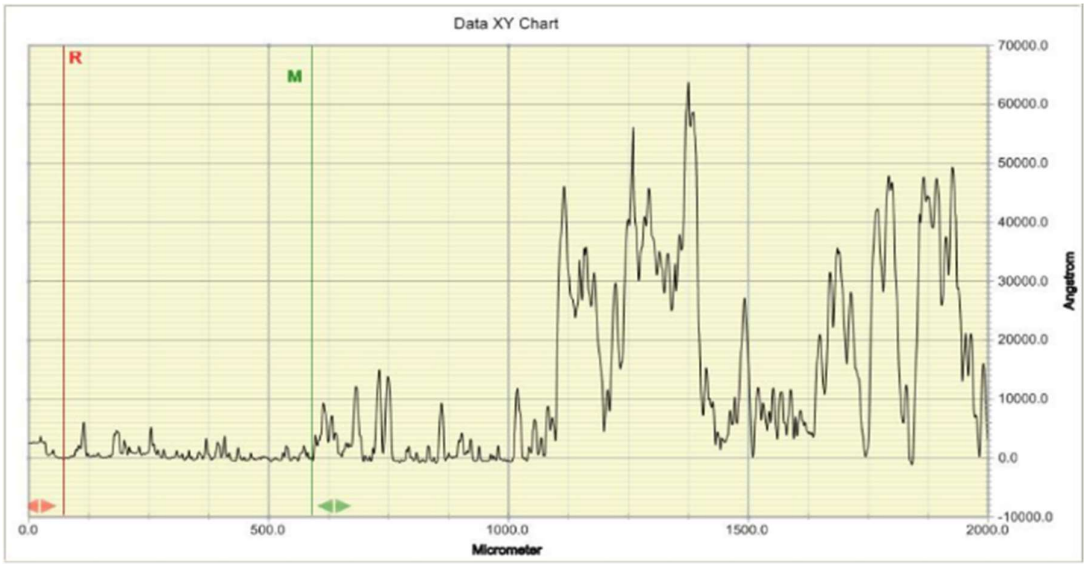


Fig. 3. Surface profilometry profile of the hydrothermally synthesized MoS_2 film, showing the substrate-to-film height variation, an estimated film thickness of approximately 3.0 µm, and the corresponding surface topographical fluctuations.

C. UV-Vis optical analysis

Fig. 4(a) compares the UV-Vis-NIR absorbance spectra of MoS_2-N_2 and MoS_2-Ar over the displayed 300-1000 nm interval spanning the UV to near-infrared spectrum. Both samples exhibit their strongest measured response toward the ultraviolet region, followed by a reduction and weaker spectral variation in the visible-near-infrared range. Across most of the plotted region, the N_2-treated sample has the higher absorbance. This behaviour could be due to improved crystallinity, as evidenced by the increase in crystallite size from the XRD [27]. Annealing in an inert atmosphere can control the concentration and distribution of structural defects, such as sulfur vacancies, crystallinity, and the local bonding environments [28]. The Ar-treated sample has higher measured transmittance, as shown in Fig. 4(b). This inverse trend follows the measured attenuation of transmitted light.

The apparent absorption coefficient, α, was evaluated from absorbance A and film thickness t using (8) [27]. For this relation to yield a physically comparable absolute coefficient (cm^{-1}), t must be known in centimetres, and the films should have comparable scattering and reflectance. As the drop-cast optical-film thickness was reported to be 0.0003 cm, the plotted α values in Fig. 4(c) establish the estimated material constant; both the annealed samples have larger apparent α, on the order of 10^4 cm^{-1}, particularly at higher photon energies. Therefore, the estimated optical values were derived considering the possible scattering, reflection, and film non-uniformity effects of the drop-cast films used due to the physical property limitations. Structural irregularities may produce additional light scattering and reflection at the film-substrate interface that may affect the measured optical absorbance.

$$\alpha = \frac{2.303A}{t} \quad (8)$$

Here A denotes the absorbance, and t is the optical-film thickness (0.0003 cm). The factor 2.303 converts dedicated absorbance to the natural-logarithm attenuation coefficient. Fig. 4(c) plots the estimated α versus photon energy hν, while Fig. 4(d) shows the corresponding extinction coefficient, k, as a function of photon energy. The larger estimated absorption coefficient of MoS_2-N_2 is consistent with its higher recorded absorbance. However, crystallite-size changes alone cannot explain the magnitude of this optical difference because the effective light path length and optical scattering of the deposited layers were not independently quantified. Annealing-related surface states, aggregation, and differences in film coverage may also affect the measured response. The observed reduction in transmittance for MoS_2-N_2 follows from its higher attenuation relative to the Ar-treated sample. In a purely absorbing, non-scattering medium, absorbance and transmittance are related through $A = -\log_{10}(T)$, where T is the fractional transmittance. For nanoparticle-derived coatings, reflection and scattering may additionally contribute to apparent optical losses. The optical extinction coefficient k, which is dimensionless and represents the imaginary component of the complex refractive index, is related to the absorption coefficient through (9).

$$k = \frac{\alpha\lambda}{4\pi} \quad (9)$$

where λ is the wavelength of incident light, expressed in units consistent with α.

As shown in Fig. 4(d), k is higher for the N_2-treated sample across much of the displayed photon-energy interval, mirroring the α trend because $k = \alpha\lambda/(4\pi)$. The apparent direct-transition optical gap was estimated using the Tauc-type relation in (10) by extrapolating the selected linear region of $(\alpha h\nu)^2$ against hν to the photon-energy axis. This analysis assumes a direct allowed transition and an adequately

characterized absorption coefficient; a direct-gap fit does not by itself establish that the entire multilayer material possesses a direct fundamental bandgap.

$$(\alpha h\upsilon)^2 = B(h\upsilon - Eg) \quad (10)$$

The Tauc plots in Fig. 5 give an apparent direct-transition optical gap of approximately 1.62 eV for MoS_2-N_2 and 1.80 eV for MoS_2-Ar, which aligns with the literature for layered MoS_2 [21], [29]. The higher bandgap in N_2-MoS_2 indicates that the nitrogen annealing atmosphere has little effect on the electronic structure of MoS_2. The difference may involve interlayer coupling, structural disorder, defect-related absorption tails, or fit-range and thickness uncertainty [30]. Annealing under N_2 conditions has the potential to change the concentration of the sulfur-related defects and localized electronic states, which may decrease the energy needed for optical excitation. The same behaviour is also seen in annealing of TiO_2 in nitrogen and argon atmospheres, as reported in [30].

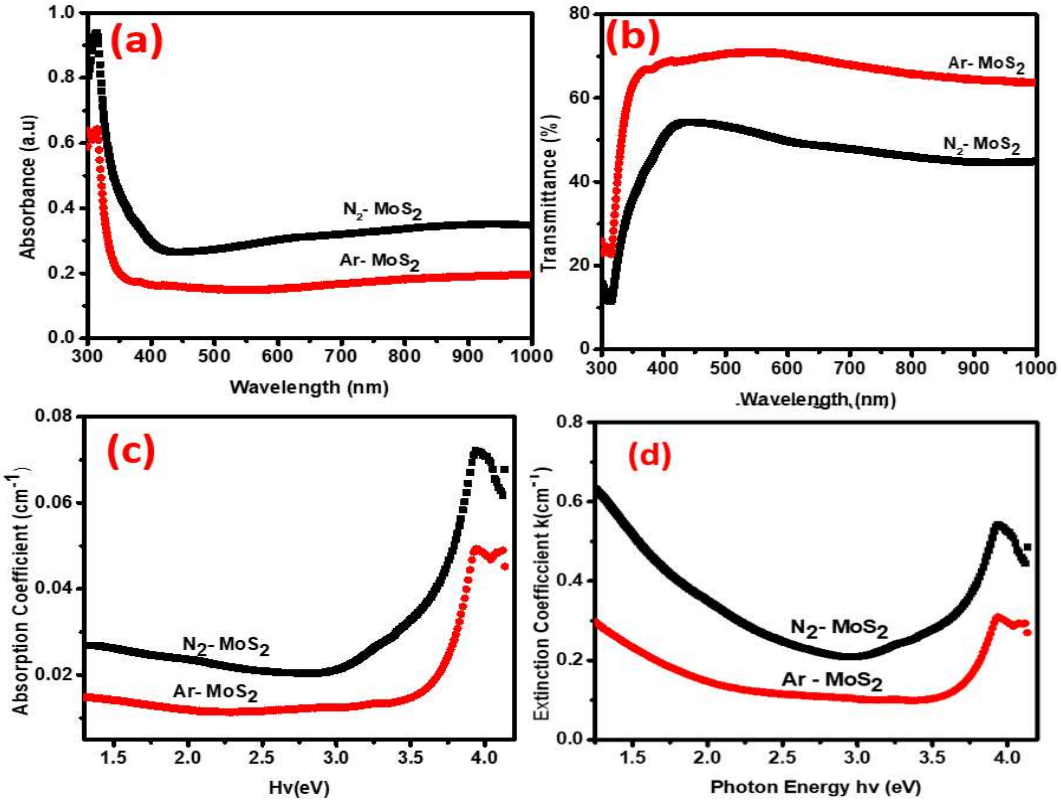


Fig. 4. Optical response of MoS_2-N_2 and MoS_2-Ar: (a) absorbance and (b) transmittance versus wavelength; (c) estimated absorption coefficient and (d) extinction coefficient versus photon energy.

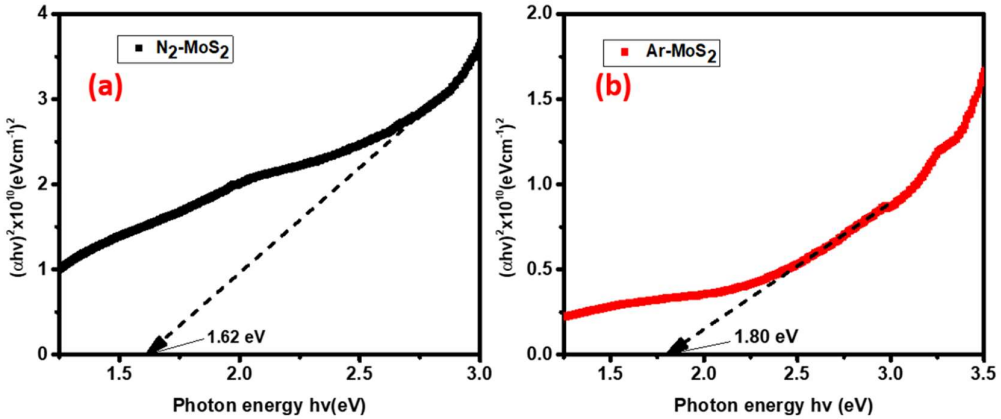


Fig. 5. Tauc plots showing the estimated direct-transition optical gaps of (a) MoS_2-N_2 and (b) MoS_2-Ar.

D. Raman spectroscopic analysis

Raman spectroscopy provides a complementary probe of lattice dynamics and interlayer coupling in 2H-MoS_2. Fig. 6 shows two characteristic first-order phonon modes for both annealed powders: the in-plane E^1_{2g} mode at 383.2 cm^{-1} (N_2) and 383.1 cm^{-1} (Ar), and the out-of-plane A_{1g} mode at 408.1 cm^{-1} in both cases (Table II) [22]. The frequency differences, $\Delta\omega = \omega(A_{1g}) - \omega(E^1_{2g})$, are 24.9 and 25.0 cm^{-1} for MoS_2-N_2 and MoS_2-Ar, respectively. Separations approach 25 cm^{-1} [6]. Table II records a higher A_{1g} peak intensity for MoS_2-Ar (2230 a.u.) than for MoS_2-N_2 (1180 a.u.), with slightly narrower reported linewidths for the Ar-treated powder (3.04 and 3.57 cm^{-1}) than for the N_2-treated powder (3.10 and 3.61 cm^{-1}). The small linewidth changes could involve phonon scattering, size, or strain. The close agreement of the mode frequencies indicates retention of similar lattice-vibrational character in both annealing environments for MoS_2 nanopowder.

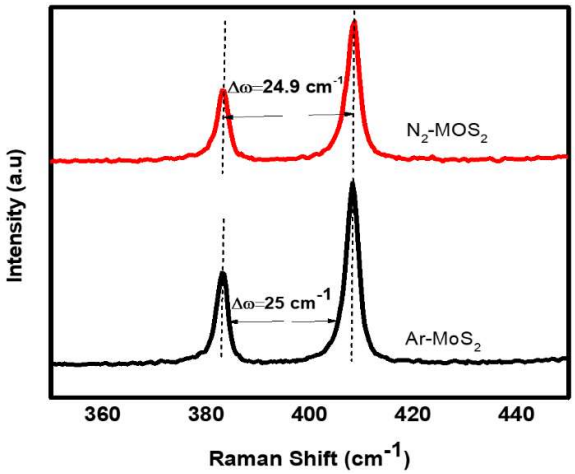


Fig. 6. Raman spectra of MoS_2 nanopowders annealed under N_2 and Ar, showing their principal in-plane and out-of-plane phonon modes.

Table II. Raman peak positions, separation, intensity, and linewidths for N_2- and Ar-annealed MoS_2 nanopowders.

Annealing atmosphere	E^1_{2g} (cm^{-1})	A_{1g} (cm^{-1})	Δω (cm^{-1})	A_{1g} intensity (a.u.)	FWHM (cm^{-1}), E^1_{2g}/ A_{1g}
N_2-MoS_2	383.2	408.1	24.9	1180	3.10, 3.61
Ar-MoS_2	383.1	408.1	25.0	2230	3.04, 3.57

E. FTIR spectroscopic analysis

Fig. 7 compares the FTIR spectra of MoS_2-N_2 and MoS_2-Ar. The N_2-treated sample displays reported features near 460, 550, 1090, 1441 and 1612 cm^{-1}, whereas the Ar-treated sample exhibits bands near 490, 611, 1099 and 1632 cm^{-1}. Features in the low-wavenumber region around 460–490 cm^{-1} are consistent with Mo-S-related lattice vibrations, supporting the XRD and Raman identification of MoS_2 [1], [31]. The changes in the positions and relative prominence of these bands indicate differences in local vibration environments.

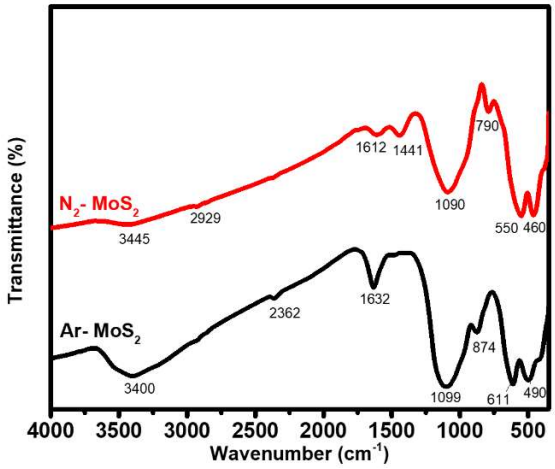


Fig. 7. FTIR transmittance spectra of N_2- and Ar-annealed MoS_2 nanopowders, plotted against wavenumber (cm^{-1}).

Additional features near 550–611 and 1090–1099 cm^{-1} may arise from surface-associated molybdenum–oxygen and sulfur–oxygen or precursor-derived species [32]. The band near 1612–1632 cm^{-1} and broad absorption around 3400–3450 cm^{-1} are consistent with adsorbed water bending and O–H stretching, respectively. A weak feature near 2929 cm^{-1} may be associated with C–H stretching from residual organic species, whereas the feature near 2362 cm^{-1} may arise from atmospheric CO_2 rather than C–H vibration [33]. It is clear that the presence of the low-wavenumber Mo–S vibration confirms the successful formation of MoS_2

F. Morphological analysis: SEM and TEM

The SEM micrographs in Fig. 8 reveal aggregated, irregularly shaped flake-like structures in both powders. The N_2-annealed sample exhibits comparatively compact overlapping domains, whereas the Ar-annealed sample appears rougher, with wrinkled features and inter-aggregate voids. Such differences suggest that the gas environment influenced the arrangement or agglomeration of the hydrothermally formed MoS_2 during subsequent heating. The morphologies of the flakes with the layers are well preserved after inert gas annealing, which suggests that the material retains its structural integrity under the annealing conditions employed [5], [34]. Annealing can influence the competition between crystallite coarsening, neck formation, particle rearrangement, and surface-energy minimization [35]. These effects may change apparent aggregate compactness without changing the diameter of each primary crystallite in the same way.

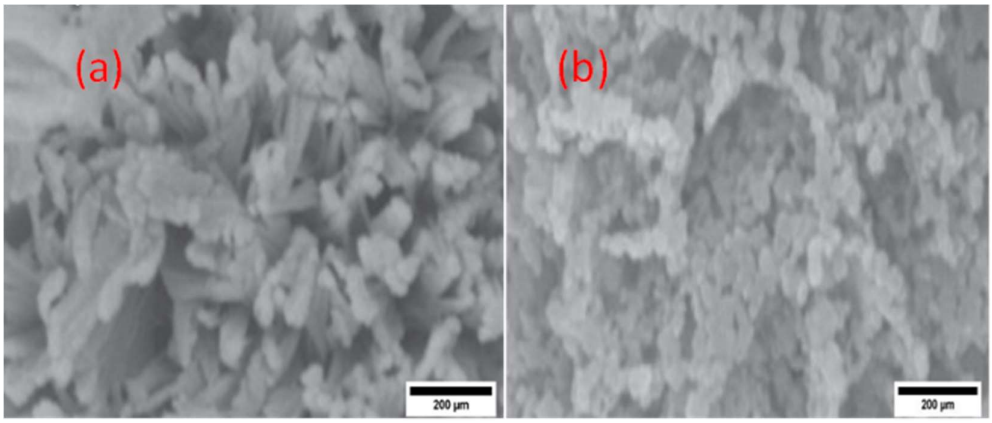


Fig. 8. SEM micrographs of MoS_2 nanopowders annealed under (a) Ar and (b) N_2.

Fig. 9 shows TEM micrographs of MoS_2-Ar and MoS_2-N_2 revealing irregular nanoscale particles and regions of interparticle contact or aggregation. TEM micrographs were used to determine the particle-size distribution with the help of ImageJ software. For each sample, at least 15 particles were analysed from several representative TEM images, and the diameter of each particle was measured. The average particle size was calculated from the measured values. The mean particle sizes are 17.97 nm for MoS_2-Ar and 13.30 nm for MoS_2-N_2. However, the estimated particle sizes may be influenced by the limited number of particles analysed, particle aggregation, image resolution, contrast variations, and the irregular morphology of some nanoparticles. Thus, the selected particles in the N_2-annealed sample appear smaller even though its mean XRD coherent-domain size (4.97 nm) is slightly larger than that of the Ar-treated sample (4.67 nm). There is no contradiction: TEM measures projected particle or aggregate dimensions, whereas Scherrer analysis estimates the extent of coherently diffracting domains, and a particle may contain multiple domains [36]. The different TEM particle sizes and SEM aggregation patterns indicate that the annealing atmosphere can affect particle-scale organization as well as atomic-scale ordering.

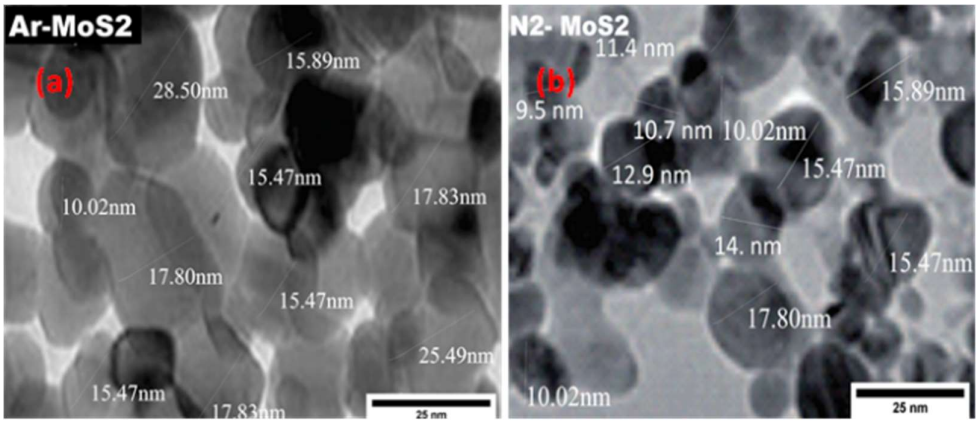


Fig. 9. TEM micrographs of MoS_2 nanopowders annealed under (a) Ar and (b) N_2.

G. Photoluminescence analysis

Fig. 10 compares the room-temperature photoluminescence (PL) spectra and excitation response of MoS_2-N_2 and MoS_2-Ar. Under an excitation wavelength of approximately 532 nm, both samples show emission features near 640 nm (1.94 eV) and 808 nm (1.53 eV), as displayed in Fig. 10(a). Under approximately 427 nm excitation, the reported features occur near 538–539 nm (about 2.30 eV) and 642–643 nm (about 1.93 eV), as shown in Fig. 10(b). In Fig. 10(c), excitation spectra were monitored at an emission wavelength of 642 nm.

The close agreement in the emission peak positions in Fig. 10(a) and (b) suggests that both annealing atmospheres preserve similar radiative recombination pathways in MoS_2, indicating that the dominant emission mechanism remains largely unchanged after annealing. The observed differences in PL intensity, however, suggest that the relative importance of radiative and non-radiative recombination processes might be altered by annealing under N_2 and Ar, which could be due to the variation in the defect states and local electronic environment. The results indicate that the optical response of MoS_2 changes depending on the annealing atmosphere but

does not cause a significant shift in the observed emission energies. In these results, it was observed that the Ar-MoS_2 sample had a significantly higher PL intensity relative to the N_2-MoS_2 sample under the same excitation conditions. PL arises from radiative relaxation of excited electronic populations; its measured intensity depends on optical absorption at the excitation wavelength, radiative and non-radiative rates, collection efficiency, film thickness, and scattering. Therefore, the weaker N_2 emission does not uniquely demonstrate suppressed total electron–hole recombination or increased carrier separation: stronger non-radiative loss, different absorption, or changes in emitting-state populations are alternative explanations. Time-resolved PL, absolute PL quantum yield, and controlled optical-density measurements would help distinguish these possibilities in future work [37]. The relatively low-energy emission near 808 nm reflects localized, defect-associated or indirect-transition-related recombination. The approximately 1 nm difference between the 642 and 643 nm emission features corresponds to only about 3 meV. In the excitation spectra monitored near 642 nm, features around 427–429 nm correspond to photon energies of approximately 2.90–2.89 eV. These small differences are consistent with subtle changes in the local electronic environment, interlayer interactions, or disorder.

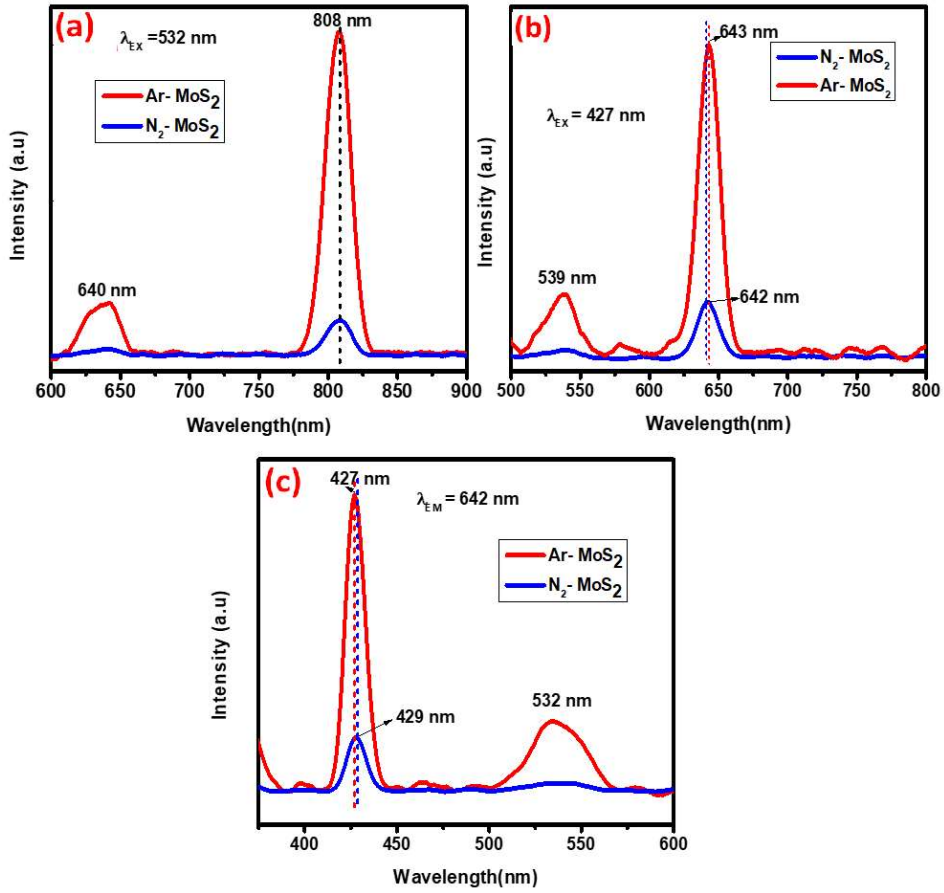


Fig. 10. Room-temperature PL response of MoS_2-N_2 and MoS_2-Ar: (a) emission spectra under 532 nm excitation; (b) emission spectra under approximately 427 nm excitation; and (c) excitation spectra monitored at an emission wavelength of 642 nm.

IV. Conclusion

Hydrothermal synthesis followed by annealing under nitrogen or argon produced MoS_2 nanopowders exhibiting the characteristic diffraction and Raman features of layered semiconducting 2H-MoS_2. XRD analysis indicated a modest increase in the mean Scherrer crystallite size from 4.67 nm for MoS_2-Ar to 4.97 nm for MoS_2-N_2, accompanied by a reduction in the (002) interplanar spacing from 6.223 to 6.042 Å. The Raman peak separations of 25.0 cm^{-1} for MoS_2-Ar and 24.9 cm^{-1} for MoS_2-N_2 are consistent with a multilayer or bulk-like vibrational response but do not establish a change in layer number.

SEM analysis revealed aggregated, flake-like morphologies, while TEM measurements of selected particles yielded mean sizes of 17.97 nm for MoS_2-Ar and 13.30 nm for MoS_2-N_2. These results highlight the distinction between atomic-scale coherent diffraction domains and particle-scale

dimensions, which may respond differently to the annealing conditions.

Optical characterisation showed higher measured absorbance and a smaller apparent direct-transition optical band gap for MoS_2-N_2 (approximately 1.62 eV) than for MoS_2-Ar (approximately 1.80 eV). In contrast, the Ar-treated sample exhibited higher PL intensity, indicating an atmosphere-dependent difference in the measured photoluminescence response. However, this observation alone does not establish more efficient charge separation or identify the dominant recombination mechanism in either material.

Overall, the findings demonstrate that the N_2/Ar annealing atmosphere is an important processing variable that can influence the measured structural, morphological, and optical properties of hydrothermally prepared MoS_2 nanopowders. Further investigations should include more precise determination of optical-film thickness and uniformity, correction for instrumental diffraction broadening, quantitative analysis of composition and defect states (e.g., using X-ray photoelectron spectroscopy), and time-resolved PL measurements to provide further insight into the underlying mechanisms. The prepared materials may have potential for applications such as the hydrogen evolution reaction, although their performance in this application requires direct electrochemical evaluation.

CRediT Authorship Contribution Statement

Bunmi J Akeredolu: Writing – original draft, methodology, investigation, formal analysis, data curation, conceptualization. John F Wansah: Writing – review and editing, validation, investigation, visualization, supervision, resources, project administration. Sani Yusuf: Writing – review and editing, visualization, validation, formal analysis, data curation, conceptualization. Michael O Awoji: Writing – review and editing, visualization, validation, formal analysis. Eli Danladi: Writing – review and editing, visualization, validation, formal analysis. Michael B Ochang: Data curation, software, resources, investigation. Asabe M Magomya: Writing – review and editing, visualization, validation. Peverga R. Jubu: Writing – review and editing, visualization, methodology, validation. Lehlohonolo F Koao: Writing – review and editing, visualization, methodology, validation, supervision, resources.

Declaration of Originality and Author Approval

The authors confirm that this manuscript is original and has been prepared with ethical integrity. All authors have read and approved the final version of the manuscript.

Declaration of Competing Interests

The authors declare that they have no known competing financial interests or personal relationships that could have appeared to influence the work reported in this paper.

Data Availability

The data supporting the findings of this study are available from the corresponding author upon reasonable request.

Acknowledgements

The authors gratefully acknowledge the Tertiary Education Trust Fund (TETFund) for supporting this research project under the 2021–2025 Intervention Programme. The authors also acknowledge the Federal University Wukari, Taraba State, Nigeria, for its institutional support.

References

[1] W. Feng et al., "Flower-like PEGylated MoS_2 nanoflakes for near-infrared photothermal cancer therapy," Scientific Reports, vol. 5, no. 1, Art. no. 17422, Dec. 2015, doi: 10.1038/srep17422.

[2] Y. Guo et al., "Mesoporous iron-doped MoS_2/$CoMo_2S_4$ heterostructures through organic–metal cooperative interactions on spherical micelles for electrochemical water splitting," ACS Nano, vol. 14, no. 4, pp. 4141–4152, Apr. 2020, doi: 10.1021/acsnano.9b08904.

[3] J. Theerthagiri, S. J. Lee, A. P. Murthy, J. Madhavan, and M. Y. Choi, "Fundamental aspects and recent advances in transition metal nitrides as electrocatalysts for hydrogen evolution reaction: A review," Current Opinion in Solid State and Materials Science, vol. 24, no. 1, Art. no. 100805, Feb. 2020, doi: 10.1016/j.cossms.2020.100805.

[4] U. Krishnan, M. Kaur, K. Singh, M. Kumar, and A. Kumar, "A synoptic review of MoS_2: Synthesis to applications," Superlattices and Microstructures, vol. 128, pp. 274–297, Apr. 2019, doi: 10.1016/j.spmi.2019.02.005.

[5] E. Pitthan, E. R. F. Gerling, T. O. Feijó, C. Radtke, and G. V. Soares, "Annealing response of monolayer MoS_2 grown by chemical vapor deposition," ECS Journal of Solid State Science and Technology, vol. 8, no. 4, pp. P267–P270, 2019, doi: 10.1149/2.0061904jss.

[6] O. Samy, S. Zeng, M. D. Birowosuto, and A. El Moutaouakil, "A review on MoS_2 properties, synthesis, sensing applications and challenges," Crystals, vol. 11, no. 4, Art. no. 355, Mar. 2021, doi: 10.3390/cryst11040355.

[7] V. Thennarasu, V. Jayachandran, H. J. Woo, J.-C. Wen, E. Munniappan, and S. Sangaraju, "A review on electron-transport highways via defect engineering in TMDs for hydrogen evolution reaction," Coordination Chemistry Reviews, vol. 567, pt. 1, Art. no. 218257, 2026, doi: 10.1016/j.ccr.2026.218257.

[8] K. M. Garadkar, A. A. Patil, P. P. Hankare, P. A. Chate, D. J. Sathe, and S. D. Delekar, "MoS_2: Preparation and their characterization," Journal of

Alloys and Compounds, vol. 487, nos. 1–2, pp. 786–789, Nov. 2009, doi: 10.1016/j.jallcom.2009.08.069.

[9] A. Shakery and G. R. Khayati, "Exploring the synthesis, properties, and applications of molybdenum disulfide (MoS_2): A comprehensive review," Engineering Reports, vol. 8, no. 6, Art. no. e70832, Jun. 2026, doi: 10.1002/eng2.70832.

[10] X. Zhang et al., "Strategies to improve electrocatalytic performance of MoS_2-based catalysts for hydrogen evolution reactions," RSC Advances, vol. 12, no. 28, pp. 17959–17983, 2022, doi: 10.1039/D2RA03066G.

[11] X. Zhang, S. Yuan, Y. Li, Z. Wang, and W. Feng, "Efficient and green strategy of ultrasound-assisted liquid-phase exfoliation of MoS_2 nanosheets," Langmuir, vol. 41, no. 25, pp. 15788–15795, Jul. 2025, doi: 10.1021/acs.langmuir.5c00260.

[12] M. Obaida, S. A. Hassan, M. N. Swelam, I. Moussa, N. H. Teleb, and H. H. Afify, "Phase manipulation of two-dimensional MoS_2 nanostructures," Bulletin of Materials Science, vol. 46, no. 1, Art. no. 40, Feb. 2023, doi: 10.1007/s12034-023-02891-w.

[13] T. Setianingsih and E. F. Ewies, "Hydrothermal methods in synthesis of inorganic materials," ChemEngineering, vol. 10, no. 8, Art. no. 103, 2026, doi: 10.3390/chemengineering10080103.

[14] P. Berwal et al., "Hydrothermal synthesis of MoS_2 with tunable band gap for future nano-electronic devices," Inorganic Chemistry Communications, vol. 159, Art. no. 111833, Jan. 2024, doi: 10.1016/j.inoche.2023.111833.

[15] D. S. Parmar et al., "An exploration of MoS_2 nanoparticles synthesized by hydrothermal method for potential application as an NIR photodetector," Materials Chemistry and Physics, vol. 345, Art. no. 131263, Nov. 2025, doi: 10.1016/j.matchemphys.2025.131263.

[16] B. Balan, M. E. Thomas, T. K. James, and S. Mathew, "Effect of hydrothermal reaction time on defect- and strain-engineered few-layered MoS_2 nanoflowers for tunable band gap and enhanced visible-light photocatalysis," New Journal of Chemistry, vol. 50, no. 17, pp. 7179–7195, 2026, doi: 10.1039/D6NJ00072J.

[17] D. Savchenko, M. Holiatkina, A. Prokhorov, A. Vasin, and E. Kalabukhova, "Annealing-atmosphere control of paramagnetic defects in ZnO microparticles," arXiv, Oct. 27, 2026, doi: 10.48550/arXiv.2610.33870.

[18] Y. Zhu et al., "Room-temperature photoluminescence mediated by sulfur vacancies in 2D molybdenum disulfide," ACS Nano, vol. 17, no. 14, pp. 13545–13553, Jul. 2023, doi: 10.1021/acsnano.3c02103.

[19] C. Chao, P.-Y. Tsai, P.-H. Wu, R.-Y. Hong, and I.-S. Yu, "Post-annealing in ultra-high vacuum or nitrogen plasma for MoS_2 thin films deposited by magnetron sputtering," AIP Advances, vol. 14, no. 3, Art. no. 035122, Mar. 2024, doi: 10.1063/6.0003229.

[20] A. Kumar et al., "Photoluminescence enhancement of CVD-grown MoS_2 monolayer by p-type doping using oxygen annealing technique," Journal of Electronic Materials, vol. 54, no. 3, pp. 2229–2238, Mar. 2025, doi: 10.1007/s11664-024-11654-0.

[21] J. Rommelfangen, M. A. Gonzalez-Angulo, D. Pareek, L. Gütay, P. J. Dale, and A. Redinger, "Modification of monolayer MoS_2 through post-deposition treatment and oxidation for enhanced optoelectronic properties," APL Materials, vol. 12, no. 4, Art. no. 041125, Apr. 2024, doi: 10.1063/5.0189378.

[22] B. J. Akeredolu et al., "Improved liquid phase exfoliation technique for the fabrication of MoS_2/graphene heterostructure-based photodetector," Heliyon, vol. 10, no. 3, Art. no. e24964, Feb. 2024, doi: 10.1016/j.heliyon.2024.e24964.

[23] L. Luo et al., "Hydrothermal synthesis of MoS_2 with controllable morphologies and its adsorption properties for bisphenol A," Journal of Saudi Chemical Society, vol. 23, no. 6, pp. 762–773, Sep. 2019, doi: 10.1016/j.jscs.2019.01.005.

[24] Y. Tian, Y. He, and Y. Zhu, "Low-temperature synthesis and characterization of molybdenum disulfide nanotubes and nanorods," Materials Chemistry and Physics, vol. 87, no. 1, pp. 87–90, Sep. 2004, doi: 10.1016/j.matchemphys.2004.05.010.

[25] B. J. Akeredolu, E. Danladi, M. O. Awoji et al., "Effect of cascaded centrifugal speed on scalability potential of few-layer graphene via liquid phase exfoliation," Scientific Reports, 2026, doi: 10.1038/s41598-026-71425-1.

[26] M. B. Ochang et al., "Electron–phonon interaction and electron energy loss function of spray-pyrolyzed Cu_2CdSnS_4 thin films at different substrate temperatures," Nigerian Journal of Applied Physics, vol. 2, no. 2, pp. 75–89, Jun. 2026, doi: 10.62292/njap-v2i2-2026-40.

[27] M. B. Ochang et al., "Electronic polarizability, single oscillator analysis and optoelectronic properties of Cu_2CdSnS_4 nanomaterial photoabsorber layer fabricated by spray pyrolysis," Next Materials, vol. 12, Art. no. 102470, Jul. 2026, doi: 10.1016/j.nxmate.2026.102470.

[28] H. A. Borbón-Nuñez et al., "Effect of inert ambient annealing on structural and defect characteristics of coaxial N-CNTs@ZnO nanotubes coated by atomic layer deposition," Ceramics International, vol. 48, no. 20, pp. 29829–29837, Oct. 2022, doi: 10.1016/j.ceramint.2022.06.245.

[29] G. Li et al., "All the catalytic active sites of MoS_2 for hydrogen evolution," Journal of the American Chemical Society, vol. 138, no. 51, pp. 16632–16638, Dec. 2016, doi: 10.1021/jacs.6b05940.

[30] E. Blasco-Tamarit, B. Solsona, R. Sánchez-Tovar, D. García-García, R. M. Fernández-Domene, and J. García-Antón, "Influence of annealing atmosphere on photoelectrochemical response of TiO_2 nanotubes anodized under controlled hydrodynamic conditions," Journal of Electroanalytical Chemistry, vol. 897, Art. no. 115579, Sep. 2021, doi: 10.1016/j.jelechem.2021.115579.

[31] T. Nagarajan et al., "Tribological, oxidation and thermal conductivity studies of microwave-synthesised molybdenum disulfide (MoS_2) nanoparticles as nano-additives in diesel-based engine oil," Scientific Reports, vol. 12, no. 1, Art. no. 14108, Aug. 2022, doi: 10.1038/s41598-022-16026-4.

[32] M. Amini, A. Ramazani, S. A., M. Faghihi, and S. Fattahpour, "Preparation of nanostructured and nanosheets of MoS_2 oxide using oxidation method," Ultrasonics Sonochemistry, vol. 39, pp. 188–196, Nov. 2017, doi: 10.1016/j.ultsonch.2017.04.024.

[33] E. Fosso-Kankeu, M. Spiro, F. Waanders, N. Kumar, and S. S. Ray, "Hydrothermal synthesis, characterisation and adsorption testing of MoS_2-zeolite for the removal of lead in an aqueous solution," in Proc. ASETH-18, ACABES-18, and EBHSSS-18, Cape Town, South Africa, Nov. 19–20, 2018.

[34] R. Sanikop et al., "Investigation of the thermal stability of MOCVD-synthesized WS_2 monolayer films," The Journal of Physical Chemistry C, vol. 130, no. 44, pp. 15360–15369, Nov. 2026, doi: 10.1021/acs.jpcc.6c04105.

[35] W. Liu, V. Srivastava, J. M. Kurley, C. Jiang, and D. V. Talapin, "Thermal stability of semiconductor nanocrystal solids: Understanding nanocrystal sintering and grain growth," The Journal of Physical Chemistry C, vol. 126, no. 49, pp. 21136–21148, Dec. 2022, doi: 10.1021/acs.jpcc.2c07400.

[36] S. A. Hassanzadeh-Tabrizi, "Precise calculation of crystallite size of nanomaterials: A review," Journal of Alloys and Compounds, vol. 968, Art. no. 171914, Dec. 2023, doi: 10.1016/j.jallcom.2023.171914.

[37] D. Kaplan, K. Mills, J. Lee, S. Torrel, and V. Swaminathan, "Excitation intensity-dependent photoluminescence of annealed two-dimensional MoS_2 grown by chemical vapor deposition," Journal of Applied Physics, vol. 119, no. 21, Art. no. 214301, Jun. 2016, doi: 10.1063/1.4948662.